

Role of codeposited impurities during growth. I. Explaining distinctive experimental morphology on Cu(0 0 1)

Ajmi BH. Hamouda,^{1,2,*} Rajesh Sathiyarayanan,^{1,3,†,‡} Alberto Pimpinelli,^{1,4,§} and T. L. Einstein^{1,||}

¹*Department of Physics, University of Maryland, College Park, Maryland 20742-4111, USA*

²*Physics Department, Sciences Faculty of University of Monastir, 5019 Monastir, Tunisia*

³*Department of Chemical Engineering, The Pennsylvania State University, University Park, Pennsylvania 16802, USA*

⁴*Scientific Attaché, French Embassy in the US, Consulate General of France, Houston, Texas 77056, USA*

(Received 31 July 2010; revised manuscript received 16 September 2010; published 24 January 2011)

A unified explanation of the physics underlying all the distinctive features of the growth instabilities observed on Cu vicinals has long eluded theorists. Recently, kinetic Monte Carlo studies showed that codeposition of impurities during growth could account for the key distinctive experimental observations [Hamouda *et al.*, *Phys. Rev. B* **77**, 245430 (2008)]. To identify the responsible impurity atom, we compute the nearest-neighbor binding energies (E_{NN}) and terrace diffusion barriers (E_d) for several candidate impurity atoms on Cu(0 0 1) using DFT-based VASP. Our calculations show that codeposition (with Cu) of midtransition elements, such as Fe, Mn, and W, could—in conjunction with substantial Ehrlich-Schwoebel barriers—cause the observed instabilities; when the experimental setup is considered, W emerges to be the most likely candidate. We discuss the role of impurities in nanostructuring of surfaces.

DOI: 10.1103/PhysRevB.83.035423

PACS number(s): 68.55.Ln, 68.35.Dv, 81.15.Aa, 68.35.Ct

I. INTRODUCTION

Spontaneous pattern formation through kinetically controlled epitaxial growth provides a viable route for nanostructuring of surfaces. A thorough understanding of atomistic mechanisms along with the knowledge of relevant surface energetics is required to realize the potential of this method. Ernst and coworkers performed STM studies of homoepitaxial growth in the step-flow mode on Cu(0 2 24) and Cu(1 1 17).^{1–3} Both surfaces have 2.17-nm-wide (0 0 1) terraces separated by open ⟨1 0 0⟩ (zigzag) steps on Cu(0 2 24) and close-packed ⟨1 1 0⟩ steps on Cu(1 1 17). The results of their experiments can be summarized as follows: (i) in the 250–400 K temperature range, step meandering occurs on both surfaces for deposition flux between 7.5×10^{-4} and 1×10^{-2} ML/s (monolayer per second) [the meandering wavelength (λ_m) scales with the deposition rate (F) as $\lambda_m \sim F^{-\gamma}$ with an exponent $\gamma = 0.17$ on Cu(0 2 24) and 0.21 on Cu(1 1 17)]; (ii) both close-packed ⟨1 1 0⟩ and open ⟨1 0 0⟩ steps undergo meandering instability; and (iii) when deposition is continued beyond 10 MLs at higher flux ($F > 1 \times 10^{-2}$ ML/s), small pyramids appear on the surface.^{3,4}

Caused by the presence of a sizable Ehrlich-Schwoebel (ES) barrier,^{5,6} the Bales-Zangwill (BZ) instability⁷ is the most common instability mechanism. It predicts $\gamma = 1/2$. The experimental values of $\gamma \approx 0.2$, noted above, rule out the BZ mechanism as the possible source of instability. This failure led to the discovery of several alternate instability mechanisms.^{8–11} Most of these models^{8–10} showed that the presence of a kink Ehrlich-Schwoebel barrier is sufficient to cause step meandering. Essentially an in-plane BZ mechanism, the instability caused by the kink Ehrlich-Schwoebel effect (KESE) also predicts a power-law relation between the meandering wavelength (λ_m) and the deposition rate (F) but with $\gamma = 1/4$. Even though this value of γ is closer to the experimental observations, KESE also predicts that open ⟨1 0 0⟩ (zigzag) steps do not undergo meandering, in contradiction to experimental observations.

Subsequently, Nita and Pimpinelli¹¹ proposed a novel instability mechanism, namely the unhindered step-edge diffusion (USED), in which atoms diffuse along step edges in the presence of a vanishing or an extremely small kink ES barrier. The USED mechanism makes both close-packed ⟨1 1 0⟩ and open ⟨1 0 0⟩ steps susceptible to meandering. However, the USED mechanism fails to account for the formation of pyramids. Thus, neither KESE nor USED mechanisms could explain all the key experimental observations. Furthermore, step-edge diffusion-induced meandering dominates over ES-barrier-induced meandering only for small values of ES barrier.¹² However, low-energy electron microscopy (LEEM) experiments give an ES barrier of 0.125 eV,¹³ and a computational estimate based on the Vienna *ab initio* simulation package^{14,15} (VASP) gives an ES barrier of 0.175 eV¹⁶ for hopping down over a step edge. These results severely challenge the adequacy of applying the KESE and USED models to Cu vicinals: There was no convincing explanation for the experimental observations of Ernst and coworkers.^{1–3}

Using kinetic Monte Carlo (KMC) simulations on a standard solid-on-solid model, some of us¹⁷ showed that impurities codeposited on the surface during growth could reproduce all the experimental observations. Our simulations showed that impurity atoms could explain the observed scaling of behavior of λ_m with F as well as account for the formation of small pyramids. We considered only the case of (codeposited) substitutional impurities (impurities that sit at high-symmetry lattice sites, replacing Cu atoms). Hence, the most important energetic parameters in this model are the strengths of the Cu-Cu and Cu-impurity nearest-neighbor (NN) bond strengths (respectively $E_{\text{NN}}^{\text{Cu}}$ and E_{NN} or $E_{\text{NN}}^{\text{imp}}$ when needed for clarity) and the energy barrier (E_d) for hopping between NN sites (by terrace diffusion) for an isolated [impurity] atom on the Cu surface. By varying the strength of these energy parameters in simulations and comparing the results with experimental morphologies, some of us¹⁷ found that the observed instabilities could be caused only by those impurity

atoms for which (i) E_{NN}^{imp} is at least 1.2 times E_{NN}^{Cu} and (ii) E_d is about 1.6 times the corresponding homodiffusion barrier of a Cu adatom.

In this article, we identify the responsible impurity atom(s) through the computation of the relevant energy parameters in their model, i.e., NN binding energy (E_{NN}) and terrace diffusion barrier (E_d) for certain candidate impurity atoms using DFT^{18,19}-based VASP. In addition to providing an answer to the long-standing puzzle of growth instabilities on Cu vicinals, knowledge about those impurity atoms could be used to achieve nanostructuring of Cu vicinals. The specifics of our VASP calculations and our results for candidate impurity atoms are given in the following section. Using the computed energy parameters, we simulate the surface morphologies that would result from the codeposition of different impurity atoms with Cu in the step-flow mode. In Sec. III, we present the particulars and results of these kinetic Monte Carlo simulations. In Sec. IV we discuss in more detail our choice for the ES barrier based on VASP calculations. We include results for barriers for other atomic transport processes such as embedding and exchange for Cu and the responsible impurity atom(s). Section V offers concluding remarks.

II. VASP CALCULATIONS OF ENERGY PARAMETERS

We computed the E_{NN} and E_d values for all candidate impurity atoms using VASP^{14,15} with the all-electron (frozen core) projector augmented-wave (PAW) method.²⁰ For the exchange-correlation functional, we used the generalized gradient approximation (GGA) of Perdew, Burke, and Ernzerhof (PBE)²¹ supplied with the VASP package. The PAW-PBE potentials are expected to give more accurate results than ultrasoft pseudopotentials for systems involving transition metals with a large magnetic moment or at the left side of the periodic table (e.g., Sc–Mn).²² The lattice constant was found to be 3.64 Å from a bulk calculation using a $(1 \times 1 \times 1)$ supercell sampled by a $(15 \times 15 \times 15)$ \mathbf{k} -point mesh. We then used a $(4 \times 4 \times 14)$ supercell sampled by a $(5 \times 5 \times 1)$ \mathbf{k} -point mesh for our calculations. We modeled the Cu(0 0 1) surface using a six-atomic-layer slab. To speed up the calculations, we used a Methfessel-Paxton width of 0.2 eV.²³ Adatoms were placed on only one side of the slab. To take into account the effects of charge transfer, we set the IDIPOL tag to 3. The sum of dipole and quadrupole corrections were found to be on the order of a few meV (maximum correction = 6 meV) for all impurity atoms. Such a small correction is expected because of the few adatoms (a maximum of two) used in the calculations. Atoms in the bottom three layers were fixed in their bulk positions, and all other layers were allowed to relax until the net force on the atoms was less than 0.01 eV/Å. We set the energy cutoff for the plane-wave basis to 400 eV. The energy barrier for terrace diffusion (E_d) was calculated as the increase in energy of the configuration with the adatom at a bridge site relative to the configuration with the adatom at the lattice site. A nudged elastic band (NEB)^{24,25} calculation for the terrace diffusion of an isolated Cu atom using seven images showed that the bridge site is indeed the saddle point along the path of terrace diffusion.

In typical growth experiments, there are two possible sources of impurities: (i) elements like C, O, and S that are

TABLE I. Terrace diffusion barrier (E_d) of several impurity atoms on Cu(0 0 1) and their bond strength (E_{NN}) with a nearest-neighbor Cu atom, arranged by increasing values of E_{NN} values. These energies are computed using VASP. A positive E_{NN} value denotes an attractive bond, while a negative value denotes repulsion at NN sites. The values inside the parentheses are computed with an energy cutoff of 275 eV (rather than 400 eV) for the plane-wave basis set.

Element	E_{NN} (eV)	E_d (eV)	Characteristic
Cu	0.350	0.564 (0.563)	
O	−0.337	0.775	
C	−0.251	1.827	$E_{NN} < 0$
S	−0.119	0.900	
Ag	0.277	0.309	
Sn	0.307	0.432	$E_{NN} \lesssim E_{NN}^{Cu}$
Zn	0.312	0.314	$E_d \lesssim E_d^{Cu}$
Al	0.422	0.493	
Pd	0.343	0.698	
Ni	0.384	0.795	$E_{NN} \approx E_{NN}^{Cu}$
Si	0.386	0.862	$1.2 \lesssim E_d/E_d^{Cu} \lesssim 1.5$
Co	0.414	0.891	
Fe	0.444	0.909 (0.902)	$1.2 \lesssim E_{NN}/E_{NN}^{Cu} \lesssim 1.8$
Mn	0.474	0.879 (0.872)	
W	0.639	0.913 (0.895)	$E_d \approx 1.6 \times E_d^{Cu}$

present in the vapor phase and (ii) heavier metallic impurities like Fe, Sn, and Zn from the experimental apparatus, such as sample holder, heating coil, and so on. To identify the impurity atom(s) responsible for meandering and mounding instabilities on Cu vicinals, we initially chose a set of candidate impurity atoms from both groups. The computed E_{NN} and E_d values for all candidate impurity atoms are listed in Table I. On this surface, the strength of the Cu-Cu NN bond is 0.350 eV (very close to previous estimate based on VASP-GGA²⁶) and the terrace diffusion barrier for Cu atoms is 0.564 eV. Among the candidate impurity atoms, only midtransition elements have energies in the range mentioned in the introduction: the E_{NN} and E_d values of only W fall in this range; the E_d values of Fe, Mn, and Co fall in the expected range but their E_{NN} values are smaller than that expected of responsible impurity atoms. Based on the computed energies alone, W emerges as the most likely impurity atom responsible for the observed instabilities. However, other impurity atoms Fe, Mn, and Co partially satisfy the requirements of impurity atoms.

To determine whether experimentally observed morphologies are obtained for all midtransition metallic impurities or only for the case of W impurity, we simulated surface morphologies when 2% of these impurities are codeposited with Cu. We obtain the experimentally observed morphologies for Fe, Mn, and W. Note $E_{NN}^{Fe} \approx 1.3 \times E_{NN}^{Cu}$ while $E_{NN}^W \approx 1.8 \times E_{NN}^{Cu}$, spanning the earlier estimate¹⁷ that $E_{NN}^{imp} \sim \frac{5}{3} E_{NN}^{Cu}$. The spread is much narrower for E_d : $E_d^{Fe} \approx 1.6 \times E_d^{Cu} \approx E_d^W$. We return to the issue of the most likely impurity atom among Fe, Mn, and W in the next section.

We can broadly classify all candidate impurities into four sets, based on their values of E_{NN} and E_d : (i) atoms that do not form NN bonds with Cu ($E_{NN} < 0$): O, C, and S; (ii) atoms whose E_{NN} and E_d values are smaller than those of Cu: Ag, Sn,

Zn, and Al;²⁷ (iii) atoms with $E_{\text{NN}} \approx E_{\text{NN}}^{\text{Cu}}$ and $E_d \gtrsim 1.25 \times E_d^{\text{Cu}}$; Pd, Ni, and Si; and (iv) atoms with $E_{\text{NN}} \gtrsim 1.2 \times E_{\text{NN}}^{\text{Cu}}$ and $E_d \approx 1.6 \times E_d^{\text{Cu}}$. A detailed discussion about the classification of impurities into sets can be found in the accompanying article.²⁸ Since the impurity atoms from the same set have comparable E_{NN} and E_d values, we expect similarities in growth morphologies obtained when two different impurity atoms from a set are codeposited (separately) with Cu. At the same time, it is reasonable to expect significant differences in surface morphologies obtained through the codeposition (with Cu) of impurities from different sets. To investigate these issues in detail, we simulated the surface morphologies obtained by the codeposition of impurities from different sets with Cu. The following section discusses our results.

III. EFFECTS ON SURFACE MORPHOLOGY OF CO-DEPOSITION OF AN IMPURITY SPECIES

We used a two-species solid-on-solid (SOS) model in our simulations and the underlying lattice was taken to be simple cubic. The two-species SOS model is an extension of the one-species model²⁹ and has been well tested by some of us in many cases.^{17,30,31,34} We used an 800×800 (in units of lattice sites) lattice with steps along the compact, close-packed direction (straight steps), separated by an average terrace width $\langle \ell \rangle = 5$ NN spacings (≈ 13 Å). To evaluate the exponent γ , we simulated growth in the presence of impurities over a wide range of flux (F) values: $F = 0.005, 0.01, 0.05, 0.1, 0.5$ ML/s. Deposition was continued up to a coverage (θ) of 40 ML before the meandering wavelength (λ_m) was measured. A small concentration (2%) of impurity atoms were codeposited with Cu atoms. A 2% impurity concentration might seem higher than the nominal impurity concentration in epitaxial growth experiments. However, our primary aim here is to identify the impurity atom responsible for the observed growth instabilities rather than to replicate experimentally observed morphologies. Also, a higher concentration of impurities enhances impurity effects and facilitates the comparison between surface morphologies obtained with different impurities.

Growth occurs via two processes: random deposition of atoms onto the substrate and surface migration. Anisotropic diffusion near step edge is also included via the ES barrier. Surface migration rates are determined by an Arrhenius expression for the first nearest-neighbor hopping probability:

$$p(E_b, T) = p_0 e^{-E_b/k_B T}, \quad (1)$$

where $p_0 = 10^{13}$ Hz is the adatom vibration frequency, T is the substrate temperature, and E_b is the energy barrier for hopping. The hopping barrier (E_b) is written as the sum of two terms

$$E_b = E_d + E_a, \quad (2)$$

where E_d , as mentioned earlier, is the barrier for diffusion of a lone atom on Cu(0 0 1) and E_a incorporates the effects of local configuration of the diffusing atom

$$E_a = \sum_{\text{NN}} n_X E_{\text{NN}}^X, \quad (3)$$

where n_X denotes the number of lateral NN atoms of type X ($X = \text{Cu}, \text{impurity}$). This formulation takes into account,

in perhaps the simplest fashion, the extra energy needed to break bonds with lateral neighbors before diffusing; more detailed investigations show that there can be nonpairwise and direction-dependent effects.³⁵ The E_{NN} values for Cu-Cu and Cu-impurity atom are listed in Table I. Heretofore we have not mentioned bond strength $E_{\text{NN}}^{\text{imp-imp}}$ between two impurity atoms at NN positions. Its effect on surface morphologies was found to be insignificant in a set of sequence of trial calculations in which the value of $E_{\text{NN}}^{\text{imp-imp}}$ ranged from 0 to twice $E_{\text{NN}}^{\text{Cu}}$. This insensitivity is likely due to the small concentration of impurities; two impurity atoms are rarely found in NN positions, so the $E_{\text{NN}}^{\text{imp-imp}}$ value has no observable effect on the resultant morphologies. Only those atoms with $\sum_{\text{NN}} n_X \leq 3$ were allowed to diffuse in our simulations. The quantities E_d and E_a are to be regarded as effective diffusion barriers that incorporate in an average way both the fast processes not included explicitly in the model, as well as other factors such as the surface reconstruction. For example, the effects of surface reconstruction need not be treated explicitly but can be incorporated into the values of these effective migration parameters.²⁹ For atoms diffusing across a step edge, an additional ES barrier (E_{ES}) about half the strength of E_{NN} for Cu is added to E_b for both Cu and impurity atoms in the simulations. In the case of Cu, this value ($E_{\text{ES}} = 0.175$ eV) is very close to a previous calculation of E_{ES} using VASP.¹⁶ To avoid distraction, we defer further discussion of E_{ES} till Sec. IV.

One of the main challenges in simulating epitaxial growth is developing a model with few free parameters, while retaining the essential features of the kinetics. As a result, certain reasonable assumptions are normally made in growth simulations. In our minimal model, we assume no preferential adsorption of impurities at step edges; therefore, impurities do not decorate the island edge as seen in the simulations of Kotrla *et al.*³⁶ We neglect both the kink ES barrier⁸ and preferential diffusion along the step edge¹¹ because neither the KESE nor the USED mechanisms could explain all the experimental observations. While both aspects are doubtless important for a full treatment of the system, our goal, again, is to find the simplest model that reproduces the observed behavior during the epitaxial growth on Cu(0 0 1) vicinals and to present a background of impurity effects on the growth morphology by accomplishing a comparative study between different chemical species, treated as impurities, under the same model. In the same spirit, we use a simple cubic model rather than an fcc lattice.

The E_{NN} and E_d values of Cu computed using VASP are much higher than the corresponding values ($E_{\text{NN}} = 0.15$ eV and $E_d = 0.4$ eV) used in the simulations of previous study.¹⁷ Accordingly, no significant adatom motions were observed in the experimental temperature range. In order to simulate growth in the step-flow mode, the temperature was raised to 425 K in the simulations.³⁷ The raising of the temperature in simulations is reasonable because atoms deposited on surfaces during molecular-beam epitaxy initially possess kinetic energy that could help them overcome such high barriers at lower temperatures, the so-called ‘‘transient-mobility.’’^{38,39}

We carried out simulations of the growth morphology for most of the impurities listed in Table I, at least two from each set. Since the E_{NN} and E_d values of impurities in a

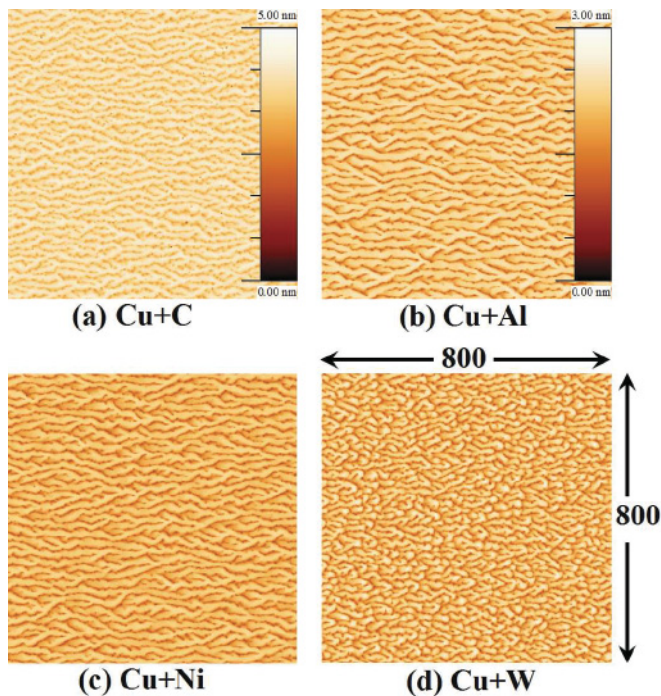


FIG. 1. (Color online) Surface morphologies from our kinetic Monte Carlo simulations after deposition, at $T = 425$ K, of 40 MLs at the experimental flux $F = 0.05$ ML/s of Cu with 2% of (a) C, (b) Al, (c) Ni, and (d) W impurity atoms. The color scheme covers a height range of 0–5 nm in (a) and 0–3 nm in all other panels. The lateral dimensions are the same as in Fig. 3. Similar morphologies are obtained if a particular impurity is replaced by another impurity from the same set.

set are close, we expect, and indeed find, similar growth morphologies for two different impurities from the same set, with modest variations attributable to the small differences in the two characteristic energies. The surface morphologies of a member of each set are shown in Fig. 1, and the corresponding values of the exponent γ , obtained from a log-log plot of λ_m vs. F , for these four impurity atoms are listed in Fig. 2.

When Cu atoms are deposited without impurity atoms, we observed layer-by-layer growth without mounding. The dependence of morphology on flux is shown in Fig. 3. The γ

value obtained for pure Cu 0.45 ± 0.05 (cf. Fig. 2) is very close to the BZ instability value. The surface morphology obtained after deposition of 40 ML of Cu atoms with 2% of C impurity atoms is shown in Fig. 1(a). From the figure it can be seen that no mounds are formed in the presence of C impurities, and there is very little variation in the height of the surface. Morphologies obtained while doping Cu with other impurities in this set are very similar to the one shown in Fig. 1(a). Since S was a well-known impurity in Cu samples during the time this set of experiments was performed, the sample was desulfurized carefully⁴⁰; hence, sulfur could not have caused the instabilities, which is consistent with our results. These results conclusively show that vapor phase impurities are not responsible for the growth instabilities on Cu observed in experiments.

Similar to the case of pure Cu, smooth layer-by-layer growth occurs when Al is codeposited with Cu and the γ value (0.50 ± 0.06) is slightly higher than that for pure Cu, while the meandering wavelength λ_m (Al) is slightly less than λ_m (Cu) [cf. Fig. 4(a)]. Also, no mounds form when any impurity atom from this set, Ag, Sn, Zn, or Al, is codeposited on the surface during growth [see Fig. 1(b)]. The surface morphology obtained with Ni impurity [cf. Fig. 1(c)] is similar to the one obtained with Al impurity, with λ_m (Ni) less than λ_m (Al). However, the extracted value of γ for Ni is notably smaller compared to the corresponding value obtained with Al impurities, and the meandering is smaller (even more so in comparison with Zn impurities). Once again, no mounds were observed to form for Ni, Pd, or Si impurities and the γ value for Ni (cf. Fig. 2) is much higher than observed in experiments.

When W is codeposited with Cu, the surface morphology [see Fig. 1(d)] is very similar to the one obtained in experiments [cf. Fig. 3(c) in Ref. 3]; λ_m (W) is smaller than the others considered in Fig. 4(a). In addition to that, the obtained value of γ (cf. Fig. 2) is very close to the experimentally observed values for open $\langle 100 \rangle$ steps. Similar results are obtained when W is replaced by Fe, Mn, or Co impurity. Even though the energies for Co are comparable to the of Fe, Mn, and W, fewer mounds appear during its codeposition with Cu. Whether this is due to the lower E_{NN} value of Co or due to an unsuitable temperature range in the simulations is not clear. It could also be due to the fact that the E_{NN} and E_d values for Co are close to those of Ni. A higher E_d barrier does not make a big difference,

Imp.	Cu	C (Set 1)	Al (Set 2)	Ni (Set 3)	W (Set 4)
γ	0.45 ± 0.05	0.35 ± 0.06	0.50 ± 0.06	0.41 ± 0.05	0.17 ± 0.02
Zoom View					

FIG. 2. (Color online) Rough estimate of the exponent γ ($\lambda_m \sim F^{-\gamma}$) and of the possibility of pyramid formation for pure Cu and for Cu codeposited with a member of each of the four sets of impurities, the impurity being 2% of the flux. Simulations are done for five values of F : 0.005, 0.01, 0.05, 0.1, 0.5 ML/s.⁴¹ For pure Cu (Cu-Cu) γ is consistent with the Bales-Zangwill⁷ value ($\gamma = 0.5$) while for Cu-W ($\gamma = 0.17$) it is in the range of the experiment.³ The zoomed views (color online) are 7% of images as in Fig. 1: after 40 ML are deposited with $F = 0.05$ ML/s at $T = 425$ K.

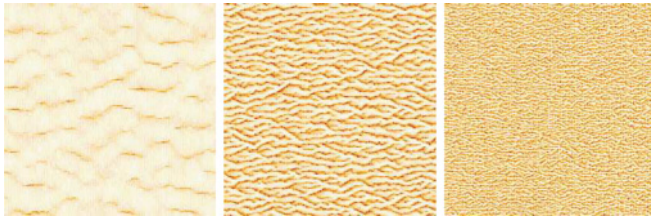


FIG. 3. (Color online) Dependence of surface morphology on flux for deposition of pure Cu: $F = 0.005, 0.05$ (used in the subsequent figures and in the actual experiment), and 0.5 ML/s; $T = 425$ K. The lateral dimensions of the panels are 800×800 in units of nearest-neighbor spacings $a(a = 2.57 \text{ \AA})$.

since impurity atoms are mostly immobile in the simulations. As a result, Co could equally well be categorized in the third set. An analysis of whether Co actually belongs to the fourth set is tangential to the goal of this study.

The zoomed views of the surface displayed in Fig. 2 also support that mounds are seen only for Set 4, containing W and Fe. To substantiate this claim, we computed the height-height correlation function $G(x, t)$ in the direction perpendicular to the steps (the x direction in ‘‘Maryland notation’’):

$$G(x, t) = \overline{\langle [h(\mathbf{r} + x\hat{\mathbf{e}}_x, t) - h(\mathbf{r}, t)]^2 \rangle}, \quad (4)$$

where the upper bar denotes a spatial average and the angular brackets a statistical-ensemble average.³¹ A similar expression can be written for the correlation function $G(y, t)$ for separations y in the direction parallel to the steps by substituting $y\hat{\mathbf{e}}_y$ for $x\hat{\mathbf{e}}_x$ in Eq. (4). From the dynamic scaling ansatz,^{32,33} we expect $G(x, t) \propto x^{2\alpha}$ for $x < \xi^{1/z}$, where α is the roughness exponent, β the growth exponent, $z = \alpha\beta$ the dynamic exponent, and ξ is the correlation length, which is slightly over twice the mean step separation of five lattice spacings according to Fig. 4(b). [For $x > \xi^{1/z}$, $G(x, t) \propto t^{2\beta}$, independent of x .] As shown (for 40 ML deposition) in

Fig. 4(b), the case for W impurities differs distinctly from the other cases, displaying a bump for x in the vicinity of ξ , while the others increase monotonically. We attribute this bump to the pyramids that occur in the case of W impurities. Unfortunately, the Ernst group apparently published no measurement of such a correlation function.

Through KMC simulations of growth using barriers computed using VASP, we have simulated surface morphologies resulting from codeposition of Cu with different impurity atoms. Our results clearly show that impurities, in conjunction with the existing BZ mechanism, significantly alter growth morphologies. Through comparison of simulated surface morphologies and the exponent γ with corresponding experimental observations, we have narrowed down the possible set of impurity atoms to Fe, Mn, and W. Further narrowing down is possible only with more information regarding the experiments. There are two possible sources of the impurities: (i) impurity atoms from the source that were activated at higher temperatures and (ii) impurities from the experimental apparatus. If the impurities really originated from the source, no further narrowing down is possible because the exact composition of the sample is very difficult to ascertain. However, if the responsible impurities originated from the experimental apparatus, then W and Fe have a higher chance than Mn of being the responsible impurity atom. In fact, a W heating element was used in the experiments.⁴⁰ Further evidence in favor of W comes from the fact that in the experiments, pyramids begin to appear only at higher deposition flux.⁴ A higher deposition flux is attained by raising the temperature of the source and an increase in the temperature of the heating element results in the evaporation of more W atoms from the wire. All of these points indicate that W atoms from the heating element are most likely responsible for the observed instabilities on Cu vicinals. (It might be interesting to investigate whether the scaling exponent γ decreases as more impurity atoms lower λ , as seen in the simulations in Ref. 17).

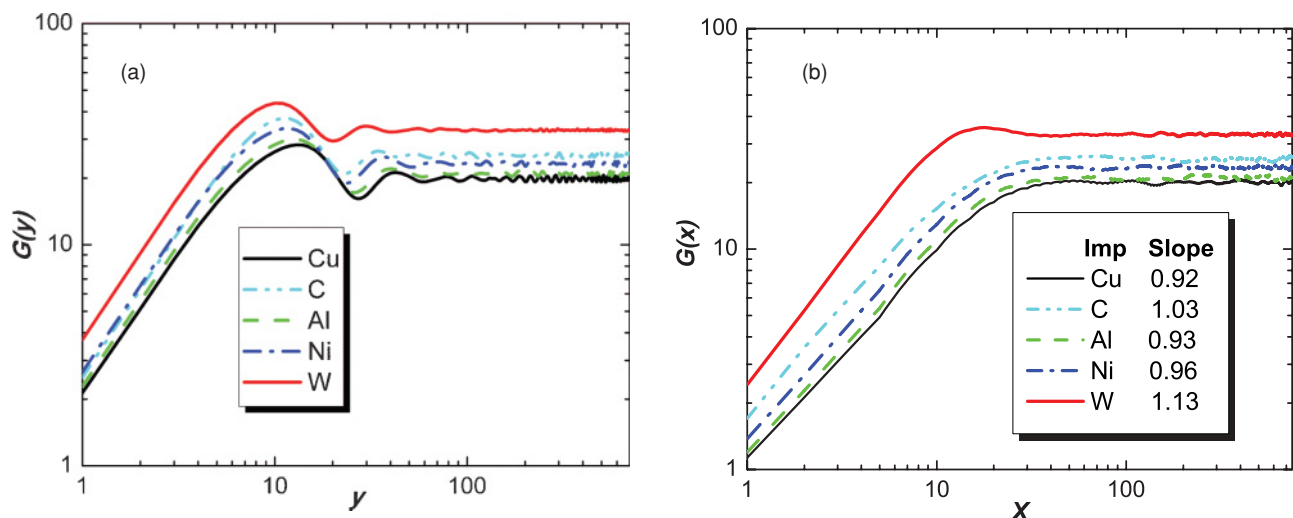


FIG. 4. (Color online) (a) Height-height correlation function (at t corresponding to 40 ML, at fixed flux $F = 0.05$ ML/s) vs. separation (in lattice spacings) in the direction parallel to the steps. $G(y)$ provides an indirect way to measure the meandering wavelength λ_m . The figure shows a progress shift of the first maximum (and minimum) to smaller y as one goes from pure Cu to W impurities, implying a corresponding decrease in λ_m . (b) Similar correlation function $G(x)$, with the same parameters, in the direction perpendicular to the steps. Only the curve for W impurities exhibits a bump in the crossover region. See text.

IV. EMBEDDING, EXCHANGE, HOPPING, AND EHRLICH-SCHWOEBEL BARRIERS

In this section, we present the results of our NEB calculations of E_d and the barrier for hopping over a step edge (E_{hop}), and thence E_{ES} from $E_{\text{ES}} = E_{\text{hop}} - E_d$, for Cu, Fe, Mn, and W, focusing our effort on the set that evidently is most relevant to the experiments under study. Also, we consider the 2 two-atom concerted diffusion mechanisms shown in Fig. 5. During embedding, an adatom displaces one of its NN substrate atoms and gets embedded in the substrate layer while the substrate atom is pushed to the adatom layer. In the exchange process, the diffusing adatom replaces one of its NN substrate atoms at the step edge, and the substrate atom is pushed to the lower terrace. The relative magnitudes of terrace diffusion and embedding barriers determine the dominant adatom diffusion mechanism on a terrace and the relative magnitudes of the hopping and exchange barriers determine the dominant adatom diffusion mechanism between neighboring terraces. Among these diffusion mechanisms, we considered only terrace diffusion and hopping over step edges in the KMC simulations of Ref. 17 and this study. It is harder to incorporate concerted two-atom processes in KMC simulations; however, we discuss below how inclusion of embedding and exchange mechanisms would modify our KMC results.

The results of our barrier calculations, based on rather standard parameter choices,⁴² are listed in Table II. Other than terrace diffusion, all of these diffusion mechanisms, with the lone exception of Cu embedding, lead to a reduction in energy of the system. We also present the magnitudes of energy

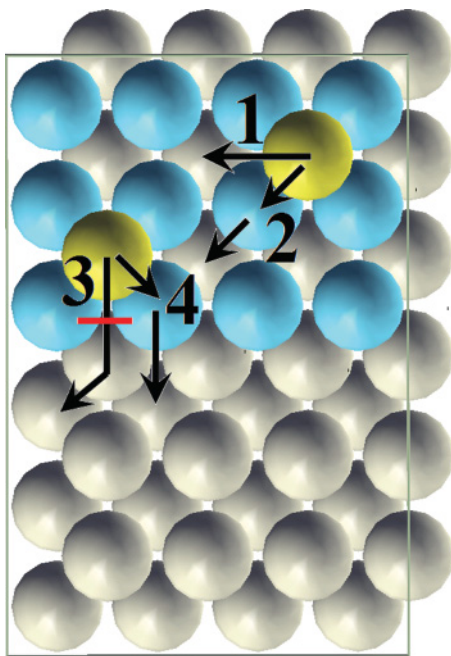


FIG. 5. (Color online) Adatom diffusion mechanisms on a (1 0 0) surface: (1) terrace diffusion, (2) embedding process, (3) hopping over a step, and (4) exchange process. The green atoms represent the diffusing adatom, the blue atoms represent the topmost layer of the substrate and the gray atoms represent atoms in the slab. The point of intersection of the hopping path (3) and the horizontal line (red line) marks the saddle point for this process.

TABLE II. Embedding, hopping, and exchange diffusion barriers for Cu, Fe, Mn, and W atoms on Cu(0 0 1) computed using VASP. The respective ES barriers are listed inside the parentheses next to the hopping barriers. The values after “/” denote the magnitude of energy reduction (initial – final energy) in the system that occurs due to these diffusion mechanisms. The sum of these two values gives the barrier for the reverse diffusion process. All energy values are given in eV. There are small differences from Table I since we use a different supercell and energy cutoff.

	E_d	E_{emb}	$E_{\text{hop}} (E_{\text{ES}})$	E_{exc}
Cu	0.550/0.0	0.695/0.0	0.695 (0.145)/0.408	0.510/0.408
Fe	0.911/0.0	0.427/0.756	1.316 (0.405)/0.544	0.295/0.980
Mn	0.865/0.0	0.397/0.863	1.334 (0.469)/0.613	0.233/1.088
W	0.880/0.0	0.262/1.690	1.845 (0.965)/0.882	0.094/1.767

reduction in the system that occurs due to these diffusion mechanisms in Table II. These magnitudes can be used to compute the energy barrier for the reverse diffusion mechanisms.

The terrace diffusion barrier (E_d) was computed using the NEB method with three images between the high-symmetry lattice site and the nearest bridge site. Since the diffusion path is symmetric, it is sufficient to sample only half of the diffusion pathway. Similar to Cu, our calculations show that, for all atoms, the bridge site is the saddle point along the diffusion pathway. The E_d values from our calculations are listed in Table II. It is clear that the terrace diffusion barriers computed using the large ($4 \times 6 \times 14$) supercell are very close to the values from ($4 \times 4 \times 14$) supercell. The trends observed in our diffusion barrier calculations are in very good agreement with the results of Mo *et al.*⁴⁴ We, too, find a linear increase in E_{hop} with increasing adsorption energy; remarkably, this holds even for W, which is in a different row of the periodic table.

To compute E_{emb} values, we sampled the diffusion pathway using five images. Except for Cu, the E_{emb} values of these elements are less than 1/2 the magnitude of their corresponding E_d values (cf. Table II). Since the E_{emb} values for all three impurity atoms are lower than the E_d values for Cu, these atoms could undergo embedding easily at the simulation temperature. For Cu, even though E_{emb} is higher than E_d , Cu atoms can still undergo embedding at the simulation temperature. Hence the embedding process becomes an important adatom diffusion mechanism on this surface.

To compute the hopping (E_{hop}) and exchange (E_{exc}) barriers, we removed three (four-atom) rows from the uppermost layer to create a three-atomic-rows-wide upper terrace (sixth layer) and lower terrace (fifth layer) (cf. Fig. 5). For both E_{hop} and E_{exc} calculations, we sampled the pathway using five images. In the case of hopping over a step, the saddle point was found to be on the upper terrace slightly beyond the step edge toward the lower terrace (cf. Fig. 5). The E_{hop} , and hence E_{ES} , values are listed in Table II. For Cu, we find E_{ES} for hopping down over a step to be 0.145 eV, close to the previous theoretical calculations¹⁶ and the value 0.175 eV used in our KMC simulations. Compared to Cu, the hopping barriers (E_{hop}) of the responsible impurity atoms, Fe, Mn, and W, are so high as to prohibit this process at the temperature range of the experiments. Hence, their presence obstructs the smooth layer-by-layer growth observed in the case of pure Cu. In the case of

the exchange process, the final configuration is about 1–1.8 eV lower than the initial configuration for impurity atoms. The E_{exc} values (cf. Table II) for all four atoms are much smaller than the respective E_{hop} values. Also, the E_{exc} values for all atoms are such that the exchange process can take place easily at the experimental temperature. Thus, the dominant mechanism for adatom diffusion from an upper terrace to a lower terrace is via exchange, and the appropriate ES barrier that should be employed in more detailed simulations (e.g., including two-atom diffusion processes) is the one associated with E_{exc} . However, for the case of pure Cu,⁴³ we find insubstantial step meandering for an ES barrier < 0.1 eV, contrary to experimental observations. Therefore, it may well be that the instabilities observed in Ernst's group's experiments are due solely to impurities, rather than a combination of impurity effects and the BZ mechanism as discussed earlier. The E_{exc} values for all three impurity atoms are much smaller than the value for Cu. This is consistent with the reasoning in Mo *et al.*⁴⁴ that the exchange barrier for adatoms that are strongly bonded to the substrate atoms should be smaller than that for weakly bonded adatoms.

In our KMC simulations including only terrace diffusion and hopping over a step mechanisms, the high E_d values render the impurity atoms, Fe, Mn, and W, immobile at the simulation temperature. However, our NEB calculations of diffusion barriers clearly show that the impurity atoms, Fe, Mn, and W, can easily diffuse through exchange and embedding mechanisms at the simulation temperature. In simulations including these mechanisms, it is reasonable to expect that due to small barriers for embedding and exchange processes in the case of responsible impurities, Fe, Mn, and W, these atoms would undergo an embedding or exchange process after deposition (this would explain why such a high concentration of impurity atoms went undetected in the experiments). Once it undergoes an embedding or exchange, the impurity atom gets lodged in a position with four NN atoms, since the barrier to escape is very large; further motion of the impurity atoms is restricted, rendering them immobile. [Nonetheless, embedded impurity atoms can still act as nucleation centers for the formation of islands, as shown in calculations for the case of Co/Cu(110).⁴⁵] Hence, except for a minor modification in the impurity atom positions, including these two processes in KMC simulations should not change our results in any significant way. However, it would be interesting to investigate the connection between the exchange process and the alignment of pyramids along the direction of a step. One of the experimental features that is absent from the KMC simulations of Ref. 17 is the alignment of the pyramids along the step direction. Our calculations show that the barrier for exchange near the step edge for these impurity atoms is very low. This combined with the fact that impurities act as nucleation centers for the growth of pyramids could explain this minor discrepancy between experimental observations and KMC simulations.

V. CONCLUSIONS

A comprehensive theoretical explanation of all the experimental observations of growth instabilities on Cu vicinals was unrealized for several years; the previously known instability mechanisms that pertain to homoepitaxial growth could not capture all observed physical features. KMC simulations-based study by some of us showed that codeposition of a small concentration of immobile impurities with Cu could explain all significant experimental features, even if it omitted some aspects (e.g., rapid edge diffusion) known to be present in this system. In this study, through computation of the energy parameters in the model using DFT-based VASP, we identify W from the heating element in the experimental apparatus as the most likely impurity atom responsible for the observed instabilities, though we cannot exclude the possibility that more than one impurity from this class (say, W and Fe) are present. We also show that the codeposition of other midtransition metallic impurities, such as Fe and Mn, could lead to similar instabilities.

Furthermore, our results show that impurity atoms codeposited during growth can significantly affect the resultant surface morphologies. Depending on their E_{NN} and E_d values relative to the corresponding values for Cu, codeposition of these impurity atoms results in specific surface morphologies. This gives the ability to tune the meandering wavelength and control the presence and density (per area) of pyramids. Thus, by computing the values of E_{NN} and E_d for any element, we can predict the morphologies that would result during the codeposition of Cu with a small concentration of atoms of that particular element. Even though this study concerns only the case of impurities on Cu, these results can be easily extended to other metallic surfaces. Our results show that by introducing the right type of impurity during growth, we can manipulate the resulting surface morphology. This is an important step toward engineering nanostructures on vicinal surfaces. From Fig. 1, it is very clear that surface morphologies obtained after 40 MLs of deposition of Cu with impurity atoms from different sets differ from each other. To explore if such differences in morphologies are already present at early stages of island nucleation, we simulated island growth in the presence of impurities in the submonolayer regime. Our results are presented in the following article.²⁸

ACKNOWLEDGMENTS

Work at University of Maryland was supported by the Maryland NSF-MRSEC, Grant No. DMR 05-20471, with ancillary support from the Center for Nanophysics and Advanced Materials (CNAM). This research was supported in part by NSF through TeraGrid resources provided by NCSA under Grant No. TG-DMR070003N. A.B.H. thanks B. Oujia for kind support of his research at Monastir. We thank T. Maroutian and J. E. Reutt-Robey for helpful interactions.

*ajmi.hammouda@fsm.rnu.tn

†srajesh@umd.edu; rajessat@in.ibm.com

‡Current and permanent address: IBM Semiconductor Research and Development Center, Bangalore 560045, India.

§On leave from LASMEA, UMR 6602 CNRS/Université Blaise Pascal, Clermont 2, F-63177 Aubière cedex, France.

¶einstein@umd.edu

‡T. Maroutian, L. Douillard, and H.-J. Ernst, *Phys. Rev. Lett.* **83**, 4353 (1999).

- ²T. Maroutian, L. Douillard, and H.-J. Ernst, *Phys. Rev. B* **64**, 165401 (2001).
- ³N. Néel, T. Maroutian, L. Douillard, and H.-J. Ernst, *J. Phys. Condens. Matter* **15**, S3227 (2003) and references therein.
- ⁴There is no sharp transition at $F \approx 1 \times 10^{-2}$ ML/s from the no-pyramids regime to one with pyramids on the surface. The experiments were done at either $F = 3 - 5 \times 10^{-3}$ ML/s or at $F = 1.8 - 2 \times 10^{-2}$ ML/s. In Refs. 2 and 3, pyramids are seen only at the higher flux range $F = 1.8 - 2 \times 10^{-2}$ ML/s. However, in Thomas Maroutian's Ph.D. dissertation (Université Paris 7, 2001, unpublished), pyramids appear at $F = 3 \times 10^{-3}$ ML/s; cf. his Figs. (3.16) and (3.18).
- ⁵G. Ehrlich and F. G. Hudda, *J. Chem. Phys.* **44**, 1039 (1966).
- ⁶R. L. Schwoebel and E. J. Shipley, *J. Appl. Phys.* **37**, 3682 (1966).
- ⁷G. S. Bales and A. Zangwill, *Phys. Rev. B* **41**, 5500 (1990).
- ⁸O. Pierre-Louis, M. R. D'Orsogna, and T. L. Einstein, *Phys. Rev. Lett.* **82**, 3661 (1999).
- ⁹M. V. Ramana Murty, and B. H. Cooper, *Phys. Rev. Lett.* **83**, 352 (1999).
- ¹⁰P. Politi and J. Krug, *Surf. Sci.* **446**, 89 (2000).
- ¹¹F. Nita and A. Pimpinelli, *Phys. Rev. Lett.* **95**, 106104 (2005).
- ¹²J. Kallunki, J. Krug, and M. Kotrla, *Phys. Rev. B* **65**, 205411 (2002).
- ¹³R. Gerlach, T. Maroutian, L. Douillard, D. Martinotti, and H.-J. Ernst, *Surf. Sci.* **480**, 97 (2001).
- ¹⁴G. Kresse and J. Hafner, *Phys. Rev. B* **47**, R558 (1993); **49**, 14251 (1994).
- ¹⁵G. Kresse and J. Furthmüller, *Comput. Mater. Sci.* **6**, 15 (1996); *Phys. Rev. B* **54**, 11169 (1996).
- ¹⁶T. S. Rahman and H. Yildirim, Proc. Am. Phys. Soc., March Meeting (Pittsburgh, 2009), abstract Q12.00007; H. Yildirim and T. S. Rahman, *Phys. Rev. B* **80**, 235413 (2009).
- ¹⁷A. Ben-Hamouda, N. Absi, P. E. Hoggan, and A. Pimpinelli, *Phys. Rev. B* **77**, 245430 (2008).
- ¹⁸P. Hohenberg and W. Kohn, *Phys. Rev.* **136**, 11169 (1964).
- ¹⁹W. Kohn and L. J. Sham, *Phys. Rev.* **140**, A1133 (1965).
- ²⁰P. E. Blöchl, *Phys. Rev. B* **50**, 17953 (1994).
- ²¹J. P. Perdew, K. Burke, and M. Ernzerhof, *Phys. Rev. Lett.* **77**, 3865 (1996).
- ²²G. Kresse and D. Joubert, *Phys. Rev. B* **59**, 1758 (1999).
- ²³M. Methfessel and A. T. Paxton, *Phys. Rev. B* **40**, 3616 (1989).
- ²⁴G. Mills, H. Jónsson, and G. K. Schenter, *Surf. Sci.* **324**, 305 (1995).
- ²⁵H. Jónsson, G. Mills, and K. W. Jacobsen, in *Classical and Quantum Dynamics in Condensed Phase Simulations*, edited by B. J. Berne, G. Ciccotti, and D. F. Coker (World Scientific, Singapore, 1998).
- ²⁶T. J. Stasevich, T. L. Einstein, and S. Stolbov, *Phys. Rev. B* **73**, 115426 (2006).
- ²⁷Even though $E_{\text{NN}}^{\text{Al}} > E_{\text{NN}}^{\text{Cu}}$, this does not change our results in any significant manner.
- ²⁸R. Sathiyarayanan, A. BH. Hamouda, A. Pimpinelli, and T. L. Einstein, *Phys. Rev. B* **83**, 035424 (2011).
- ²⁹T. Shitara, D. D. Vvedensky, M. R. Wilby, J. Zhang, J. H. Neave, and B. A. Joyce, *Phys. Rev. B* **46**, 6815 (1992); T. Shitara, T. Suzuki, D. D. Vvedensky, and T. Nishinaga, *Appl. Phys. Lett.* **62**, 1347 (1993).
- ³⁰A. BH. Hamouda, T. J. Stasevich, A. Pimpinelli, and T. L. Einstein, *J. Phys. Condens. Matter* **21**, 084215 (2009).
- ³¹A. BH. Hamouda, A. Pimpinelli, and R. J. Phaneuf, *Surf. Sci.* **602**, 2819 (2008).
- ³²A.-L. Barabási and H. E. Stanley, *Fractal Concepts in Surface Growth* (Cambridge University Press, Cambridge, 1995); P. Meakin, *Fractals, Scaling and Growth Far from Equilibrium* (Cambridge University Press, New York, 1998).
- ³³A. Pimpinelli and J. Villain, *Physics of Crystal Growth* (Cambridge University Press, Cambridge, 1999).
- ³⁴A. BH. Hamouda, A. Pimpinelli, and T. L. Einstein, *Europhys. Lett.* **88**, 26005 (2009).
- ³⁵J. A. Venables, *Phys. Rev. B* **36**, 4153 (1987); T. L. Einstein, J. Jacobsen, and C. Schiff, *Bull. Am. Phys. Soc.* **42**, 26 (1997); H. Mehl, O. Biham, I. Furman, and M. Karimi, *Phys. Rev. B* **60**, 2106 (1999).
- ³⁶M. Kotrla, J. Krug, and P. Šmilauer, *Phys. Rev. B* **62**, 2889 (2000) and references therein.
- ³⁷The temperature used in the simulations of A. B.-H. Hamouda *et al.*¹⁷ falls in the experimental temperature range. To see significant atomic motion for the case of barriers computed using VASP, we scaled the simulation temperature (compared to the temperature used in Ref. 17) by approximately the same factor as the ratio of the E_d values for Cu used in the two sets of simulations. This is reasonable because the diffusion of lone Cu atoms is the predominant atomic motion in this case.
- ³⁸W. F. Egelhoff and I. Jacob, *Phys. Rev. Lett.* **62**, 921 (1989).
- ³⁹J. W. Evans, P. A. Thiel, and M. C. Bartelt, *Surf. Sci. Rep.* **61**, 1 (2006).
- ⁴⁰Thomas Maroutian, private communications (2009); cf. Refs. 1,2.
- ⁴¹For each F only one simulation was performed. To obtain a better fit, an average over many simulations should be done for each flux. However, the trend in γ is unmistakable.
- ⁴²To compute these diffusion barriers using the NEB method in VASP, we used a $(4 \times 6 \times 14)$ supercell and sampled it with a $(4 \times 3 \times 1)$ \mathbf{k} -point mesh. We used a slab that is six atomic layers thick, with the bottom three layers fixed, and all other layers were allowed to relax until the net force on the atoms was less than $0.01 \text{ eV}/\text{\AA}$. Since Cu and the three impurity atoms are all transition metals (with the ENCUT values in the POTCAR files for all three atoms falling in the range 223–273.2 eV), we reduced the energy cut-off for the plane-wave basis set to 275 eV in these calculations. To check that reducing the energy cut-off does not affect the accuracy of the computed energy values significantly, we recalculated E_d values for Cu, Fe, Mn, and W on a $(4 \times 4 \times 14)$ supercell with an energy cutoff of 275 eV. The results are listed inside the parentheses in Table I. Since the recalculated E_d values are very close (maximum difference of 18 meV, within 2% difference) to the values computed with 400 eV cutoff, an energy cutoff of 275 eV was deemed sufficient for the barrier calculations.
- ⁴³Since both hopping and exchange lead to the same end configuration only for pure Cu, this is the only case that we could simulate with our minimal-model algorithm, which does not include two-atom concerted diffusion mechanisms.
- ⁴⁴Y. Mo, W. Zhu, E. Kaxiras, and Z. Zhang, *Phys. Rev. Lett.* **101**, 216101 (2008).
- ⁴⁵R. Pentcheva and M. Scheffler, *Phys. Rev. B* **65**, 155418 (2002); O. V. Stepanyuk, N. N. Negulyaev, A. M. Saletsky, and W. Hergert, *Phys. Rev. B* **78**, 113406 (2008).